SCIENTIFIC REPORTS
nature research

OPEN

Tuning of ionic mobility to improve the resistive switching behavior of Zn-doped CeO_2

Shania Rehman[1], Honggyun Kim[1], Muhammad Farooq Khan[1], Ji-Hyun Hur[1], Anthony D. Lee[2] & Deok-kee Kim[1*]

Correlation between the resistive switching characteristics of Au/Zn-doped CeO_2/Au devices and ionic mobility of CeO_2 altered by the dopant concentration were explored. It was found that the ionic mobility of CeO_2 has a profound effect on the operating voltages of the devices. The magnitude of operating voltage was observed to decrease when the doping concentration of Zn was increased up to 14%. After further increasing the doping level to 24%, the device hardly exhibits any resistive switching. At a low doping concentration, only isolated V_o existed in the CeO_2 lattice. At an intermediate doping concentration, the association between dopant and V_o formed $(Zn, V_o)^{\times}$ defect clusters. Low number density of these defect clusters initially favored the formation of V_o filament and led to a reduction in operating voltage. As the size and number density of $(Zn, V_o)^{\times}$ defect clusters increased at a higher doping concentration, the ionic conductivity was limited with the trapping of isolated V_o by these defect clusters, which resulted in the diminishing of resistive switching. This research work provides a strategy for tuning the mobility of V_o to modulate resistive switching characteristics for non-volatile memory applications.

As existing semiconductor technologies are approaching their physical scaling limits, a new memristive device concept[1,2] has gained great attention for its use in future highly scalable nonvolatile memories. The switching mechanism in resistive random-access memory (RRAM) is governed by the oxide ion migration and the formation of oxygen vacancy (V_o) filament within the metal oxide thin films. The ionic migration is driven by the electric field induced drift motion and concentration gradient dependent diffusion[3]. This drift/diffusion of V_o is supposed to play a key role in determining the ultimate resistive switching behavior of the devices. The ionic diffusion coefficient is expressed as $D = [V_o^{\cdot\cdot}]\gamma a^2\theta e^{(-E_m/k_BT)}$[4], where $[V_o^{\cdot\cdot}]$ is the concentration of oxygen vacancies, γ is a constant, a is the jump distance, θ is the attempt to escape frequency, E_m is the oxide ion migration energy barrier, k_B is the Boltzmann constant, and T is the temperature. The above expression makes it clear that the diffusion coefficient depends on $[V_o^{\cdot\cdot}]$ the mobility of oxygen ion via $e^{(-E_m/k_BT)}$. The mobility of the oxygen ions is directly proportional to the ionic conductivity of the oxygen ions. Hence, it can be assumed that the mobility or ionic conductivity of oxygen ions and the concentration of oxygen vacancies are the key parameters to control the resistive switching behavior in RRAM.

The ionic conductivity of pure CeO_2 used in this study is not very high because of the low concentration of oxygen vacancies[5]. However, the exceptional sensitivity of ionic conductivity of doped CeO_2 associated with doping level have been demonstrated[6,7]. The ionic conductivity of CeO_2 can be modulated by doping it with lower valency (bivalent or trivalent) cations. Theoretical studies indicate that Ce^{4+}/Ce^{3+} reduction is greatly enhanced when the CeO_2 is doped with bivalent or trivalent oxides[6]. When CeO_2 is doped with bivalent oxide, Ce (IV) atoms of host lattice are replaced with bivalent cations, and an O vacancy is formed in order to compensate the created charge. These created vacancies make the diffusion of O ions easier, and increase ionic conductivity. The formation of the oxygen vacancy results in the reduction of two neighboring Ce ions from Ce^{4+} to Ce^{3+}[7,8]. This increase in concentration of oxygen vacancies and their mobility on doping with bivalent dopant may control the characteristics of memory devices such as switching speed, operating voltage, and the R_{on}/R_{off} ratio. Although the resistive switching behavior of CeO_2 films has already been investigated[9–11], the previous studies on the resistive switching characteristics of CeO_2 has encountered the demerits of high operating voltage[12] and a low memory window[13].

[1]Department of Electrical Engineering, Sejong University, Seoul, 05006, Republic of Korea. [2]Department of Mechanical Engineering Technology, Farmingdale State College, Farmingdale, New York, 11735, USA. *email: deokkeekim@sejong.ac.kr

Different strategies such as doping[14] or interface engineering which includes the introduction of a CeO_x/silicon (Si) interface[15], ZrO_y interfacial layer[10] or the use of reactive metal electrodes[16] was adopted for the creation of oxygen vacancies in CeO_2 films to reduce the operating voltages and improve endurance. In this study, we have utilized a different approach to modulate the level of oxygen stoichiometry and defects in the CeO_2. It is known that bivalent dopants are more efficient for obtaining the lower reduction energy because the bivalent dopant may introduce twice the number of oxygen vacancies in host CeO_2 lattice as compared to trivalent dopants at the same doping level[6] (Supporting information S1). We chose Zn^{2+} (0.091 nm) as a bivalent dopant having comparable ionic radii with Ce^{4+} (0.097 nm), because it not only increases the reducibility of CeO_2[17,18], but also is economic and easily available compared to high ionic rare earth metal dopants such as Sm^{3+} and Ga^{3+}. The Zn doping level in this study was much higher as compared to previous studies, where doping was initiated by using an electric field stimulated diffusion of metal ions from an inserted metal layer[10,19,20]. However, the doping level was kept below the solubility limit[21] (20–30%) to avoid the complexity of the secondary phase evolution of ZnO in CeO_2. Based on previous studies[6,22,23], it is clear that the dopant incorporation in the CeO_2 lattice has a significant influence on the transport properties of O ions. The interactions between dopants and oxygen vacancies at higher doping levels play an important role in determining the mobility of oxygen ions. The effect of the defect interaction with oxygen vacancies on the resistive switching mechanism has rarely been reported before. At low doping levels, isolated V_o are created, which results in an increase of mobility of the oxygen ion. At medium doping levels, defect associates or clusters are formed with certain binding or association energy because of interactions between dopants and oxygen vacancies, but the number density of these defect is very low at medium doping levels to affect the mobility of oxygen ions. At higher doping concentrations, the number density of these defect associates increases and prevent oxygen vacancy from being mobile, and they consequently affect the ionic conductivity[24–26]. There are two major factors that determine the association energy of a dopant-oxygen vacancy cluster. The first factor is the Coulombic interaction that corresponds to the electrostatic attraction among the dopant ions and oxygen vacancies, and the second is the elastic interactions that refers to the size mismatch of dopants as compared to the host lattice[27–29]. Hence, the valence and ionic radius of the dopant cations play a key role in modulating the electrical conductivity of doped CeO_2. The defect chemistry of Zn-doped CeO_2 is given in the Supplementary information S2.

Experimental Details

Au was deposited as the bottom electrode by an e-beam evaporator with a thickness of 70 nm. CeO_2 and ZnO targets (Superconductor Materials (SCM), USA) were used for the deposition of the active layer in the RF sputtering unit. Prior to the deposition of CeO_2, the sputtering chamber was evacuated down to a pressure level of 2×10^{-6} Torr. During the deposition, working pressure inside the chamber was 22 mTorr. Ar and O_2 gases with the flow rates of 14 sccm and 2 sccm were introduced into the chamber. The RF-power of the CeO_2 target was kept at 150 W. The RF power of the ZnO target was varied from 35 W and 45 W to 55 W to modulate the doping level in different Zn-doped CeO_2 samples. According to the doping levels determined by XPS, the samples are labelled as $6ZnCeO_2$, $14ZnCeO_2$ and $24ZnCeO_2$ for Zn-doped CeO_2 samples deposited by the ZnO sputtering target with RF power of 35 W, 45 W, and 55 W, respectively. After deposition, samples were annealed at 500 °C for 20 minutes in an Ar environment to allow uniform doping. Finally, the top electrode of Au was deposited by an e-beam evaporator with a thickness of 70 nm and an area of $75 \times 75\ \mu m^2$ using a shadow mask. The surface composition and chemical properties were analyzed by a Thermo Fisher Scientific (with K-alpha X-ray source) X-ray photoelectron Spectroscopy (XPS). The Raman spectra were obtained using a Renishaw micro-spectrometer with a laser wavelength of 514 nm at room temperature. The spot size was ~1 μm and the power was maintained at ~1.0 mW to reduce the heating effects. The electrochemical impedance spectroscopy was performed using a ZIVE SP2 electrochemical workstation (WonATech Co., Ltd, Republic of Korea). The measured frequency ranged from 0.1 Hz to 1 MHz under a bias voltage of 10 mV. The electrical characteristics were measured using an Agilent B1500 semiconductor characterization system at room temperature.

Results and Discussion

XPS is utilized to determine the elemental composition and valence states of the Zn-doped CeO_2 samples. The detailed survey XPS spectra of un-doped CeO_2 and Zn-doped CeO_2 are shown in Figure S3(a). The spectra revealed the existence of characteristic peaks of Ce, Zn, and O. In order to calculate the elemental composition and identification of chemical states, the high-resolution O 1s, Zn 2d, and Ce 3d core level spectra are discussed in more detail below. Figure 1(a,b) display the Zn 3d XPS spectra for un-doped and Zn-doped CeO_2 in the binding energy range from 80 eV to 98 eV and from 1015 eV to 1028 eV with different concentrations of Zn controlled by changing the RF power of the ZnO target from 35 W to 55 W with an increment of 10 W. The spectra in Fig. 1(a) is de-convoluted into two peaks. On the other hand, the spectra in Fig. 1(b) is fitted with one peak. The characteristic peaks of Zn are observed at 89 eV in Fig. 1(a), and 1022 eV in Fig. 1(b), respectively. This spectrum confirmed the Zn doping in CeO_2. The Zn^{2+} concentration in each sample was estimated by adding the areas under the curves of the 89 eV and 1022 eV peaks, and dividing by the sum of the areas of all characteristic peaks multiplied by their cross-section of Ce^{3+}, Ce^{4+}, Zn^{2+} and O^{2+} in the spectra.

In order to analyze the effect of dopant on the surface chemistry and estimate the relative fraction of Ce^{4+} and Ce^{3+} oxidation states in the Zn-doped CeO_2 samples, the Ce 3d spectra was de-convoluted into eight peaks as shown in Fig. 2. The peaks at 885 eV and 903.5 eV are assigned to Ce^{3+}, while 882 eV, 898 eV, and 916.35 eV are attributed to the Ce^{4+} state[30]. The coexistence of Ce^{4+} and Ce^{3+} ions can be seen in each sample. The relative concentration of the Ce^{3+} species in each sample is calculated by dividing the sum of the integrated areas of the Ce^{3+} peaks to the total area of all the peaks (Ce^{3+} and Ce^{4+} species) in the spectrum. The calculated concentration of the Ce^{3+} ions was 14%, 21%, 26%, and 22% in un-doped CeO_2, $6ZnCeO_2$, $14ZnCeO_2$ and $24ZnCeO_2$, respectively. The analysis showed that the Ce^{3+} concentration was increasing in the samples with the increase in the

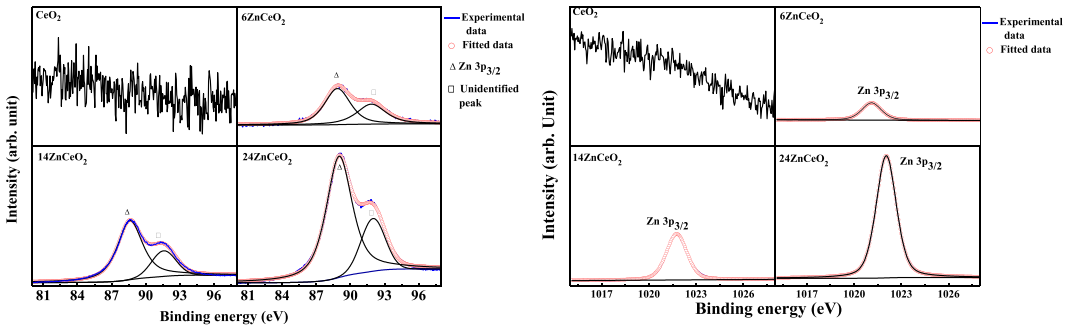

Figure 1. (**a**) High resolution XPS spectra of Zn $3p_{3/2}$ in un-doped and Zn-doped CeO_2 samples. (**b**) High resolution XPS spectra of Zn $3p_{3/2}$ in un-doped and Zn-doped CeO_2 samples.

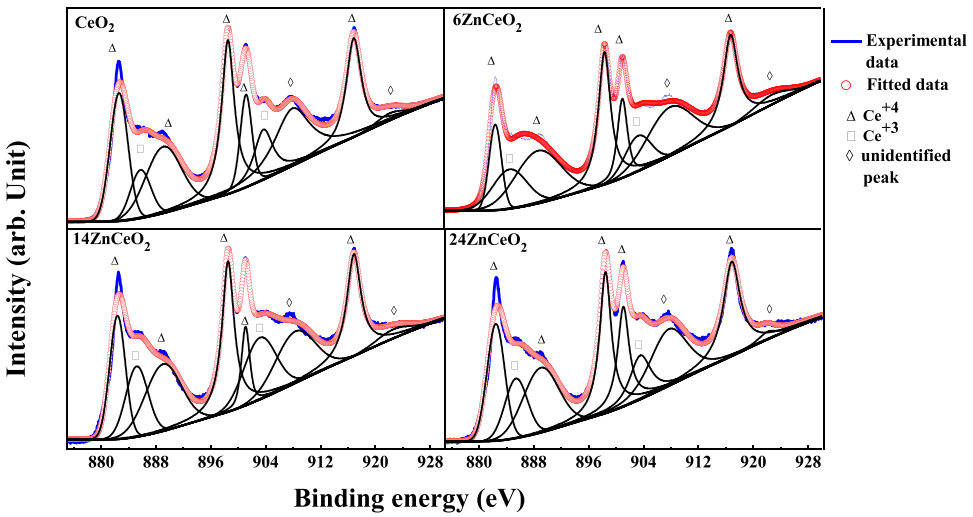

Figure 2. (**a**) High resolution XPS spectra of Ce 3d in un-doped and Zn-doped CeO_2 samples.

doping concentration. It has been reported that the presence of Ce^{3+} ions in the CeO_2 is linked with the formation of oxygen vacancies[8]. It is described in the previous section that when the CeO_2 is doped with bivalent ions, the Ce^{4+}/Ce^{3+} reduction is greatly enhanced. When the Zn dopant substitute was Ce^{4+}, an O vacancy formed inside the CeO_2 lattice. The formation of the oxygen vacancy resulted in the reduction of two neighboring Ce ions from Ce^{4+} to Ce^{3+}. Thus, the systematic increase in Ce^{3+} content in the $6ZnCeO_2$ and $14ZnCeO_2$ was an indication of more oxygen vacancies on increasing the doping concentration. However, the decrease in Ce^{3+} content was observed in the $24ZnCeO_2$ sample on increasing the dopant concentration. The slightly decreased Ce^{3+} concentration in $24ZnCeO_2$, which is unlike other doping concentrations indicated that there was a saturation of isolated oxygen vacancies at this point. At low doping concentrations, association between Ce^{4+} and V_o was strong, which resulted in the enhancement of Ce^{3+}. As the doping level increased, the association between dopant and V_o became stronger, which resulted in the formation of $(Zn, V_o)^{\times}$ defect clusters, and the preferred substitutional position of dopant was in the defect cluster $(Zn, V_o)^{\times}$. This resulted in a decrease in the reduction process of Ce^{4+} to Ce^{3+} by an interaction with nearby V_o[26].

The high-resolution O 1s core-level spectra is shown in Figure S3(b) which is de-convoluted into two peaks for further analysis. The peaks in the range of 531.0–532.6 eV can be attributed to the surface oxygen species adsorbed on the oxygen vacancies (i.e., O^-, OH^-). However, the binding energy at 529.4 eV was assigned to lattice oxygen[31]. The spectrum was composed of lattice oxygen and chemisorbed oxygen species. For analysis, we only considered the contribution of the peak associated with lattice oxygen. As it can be seen in Figure S3(b), the intensity of the peak is reduced on increasing the doping concentration. As previously discussed, increasing the doping concentration creates more oxygen vacancies. This decrease in the intensity of the peak is associated with the formation of more oxygen vacancies on increasing the doping concentration.

A Raman spectroscopy was employed to study the relative change in vibrational modes and lattice structural characteristics of CeO_2 as a function of Zn doping. Raman spectroscopy is an efficient technique to study symmetry breaking and defect associates in doped CeO_2[32]. This technique is very useful to detect the changes in the bonding atmosphere, because it allows a thorough analysis of the Ce–O bonds[32,33]. The excitation laser of wavelength 514 nm can provide information about bulk of Zn-doped CeO_2[22]. Figure 3 displays the Raman spectrum of Zn-doped CeO_2 thin films measured in the range of 400 cm^{-1} to 700 cm^{-1}. The main Raman-active mode (F_{2g})

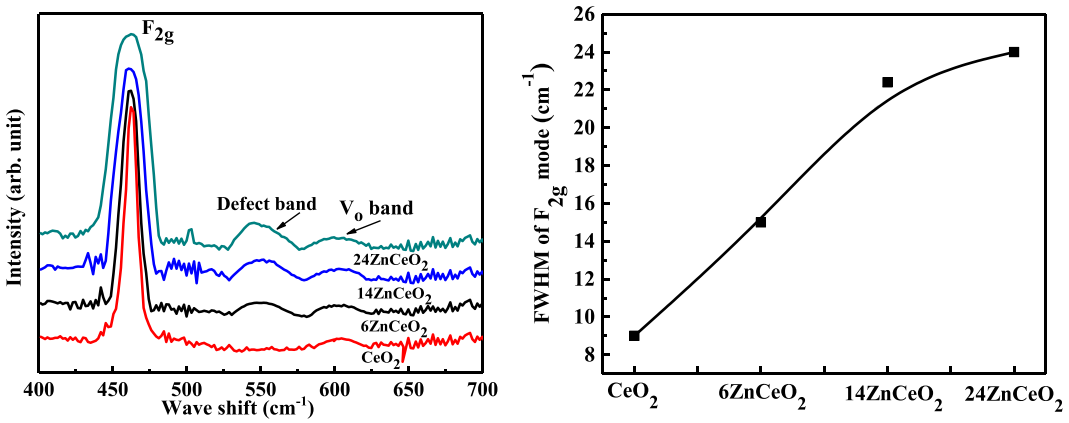

Figure 3. (**a**) Raman spectra of un-doped and Zn-doped CeO_2 samples. (**b**) Plot of variation of FWHM of F_{2g} mode in undoped and Zn doped CeO_2 samples.

in a fluorite-type CeO_2 due to Ce−O stretching vibration, is located around 462 cm^{-1} [34]. It is considered that the F_{2g} mode is assigned to the symmetric breathing mode of oxygen ions around the Ce cation, and its position is strongly dependent on the Ce (cation)-O (anion) bond strength[35]. As can be seen in the Raman spectrum of the Zn-doped CeO_2, increasing the doping concentration results in an increase in FWHM and a frequency shift of the F_{2g} peak. This increase in FWHM and a frequency shift are associated with structural disorder induced by the dopant by increasing the dopant concentration[36].

Additional modes at 555 cm^{-1} and 610 cm^{-1} were also observed in the Raman spectra. A Peak at 590 cm^{-1} originated due to oxygen vacancies and disturbed local symmetry induced by the different sizes of the dopants and a peak at 610 cm^{-1} in CeO_2 is associated with intrinsic oxygen vacancies[37,38]. In this case, different sizes of Zn^{2+} versus Ce^{4+} cations were responsible to activate the 555 cm^{-1} mode in the doped CeO_2 samples. The presence of these modes can be associated with the homogeneous incorporation of Zn within the CeO_2 crystal structure and the formation of oxygen vacancies associated with this phenomenon. The oxygen vacancy peak found in the un-doped CeO_2, can be associated with the presence of some intrinsic vacancy. As the deposition was performed in a very low O_2 atmosphere, it may also have contributed to the formation of oxygen vacancies. The enhancement of the 555 cm^{-1} mode with the increase in doping concentration was associated with the increase in oxygen vacancies and associated structural disorder on increasing doping concentration.

Electrochemical impedance spectroscopy (EIS) is employed to study the influence of doping on the ionic conductivities of the as-synthesized un-doped and Zn-doped CeO_2 samples. Generally, for the case of ionic conductivity materials, the EIS mainly consists of three arcs: the high frequency arc, the middle-frequency arc, and the low frequency tail. The high frequency arc, the middle frequency arc, and the low frequency tail correspond to the grain interior, grain boundaries, and electrode contribution to the overall conductivity of the sample[22]. Figure 4(a) shows the typical Nyquist plots for the CeO_2, $6ZnCeO_2$, $14ZnCeO_2$, and $24ZnCeO_2$ samples obtained in air. These plots, which comprised of one semicircle, were different from the typical Nyquist plots of un-doped and Zn-doped CeO_2 that consist of two separate semicircles[39]. This difference was assigned to the existence of experimental stray capacitance, which was several orders of magnitude higher than the capacitance of the bulk and grain boundaries of the film[40,41]. Since the existence of stray capacitance makes it difficult to distinguish between the contribution of grain interior and grain boundary, only the additive effect of both resistances can be measured. The equivalent circuit shown in Fig. 4(b) consists of the resistance R and a constant phase element (CPE) in parallel was used for the fitting of Nyquist plot. The CPE is the replacement of ideal capacitor. Mathematically, impedance of the CPE is defined as[42]

$$Z = \frac{1}{iw^{\alpha}C_{\alpha}}, \tag{1}$$

where i, w, and α are $\sqrt{-1}$, angular frequency and a factor associated with the deviation from ideal resistor, capacitance, and inductor. It corresponds to a resistor, a capacitor and an inductor when $\alpha = 0$, $\alpha = 1$ and $\alpha = -1$, respectively. In the actual application of this element, α is defined between 0 and 1, and this element can be assumed a generalization of a conventional capacitor. C_{α} is the constant phase element. The equivalent circuit shown in Fig. 4(b) and corresponding parameters (R and CPE) were obtained by fitting of the experimental data using ZMAN software. According to the fitted results, the values of R and CPE are listed in Table 1 and plotted in Figure S4. As is shown in Table 1 and Figure S4, the resistance of CeO_2 decreases with the increase in doping concentration up to 14%. With further increase of the doping concentration, a slight increase in the resistance of $24ZnCeO_2$ was observed. At low doping concentrations, dopant cations substitute the Ce^{4+} in the lattice structure, form a solid solution and, increases the concentration of isolated oxygen vacancies. This leads to an increase in the ionic conductivity. At intermediate doping concentrations, association between the dopant and V_o forms clusters. Both the size and number density of these clusters increases with the doping concentration. For high

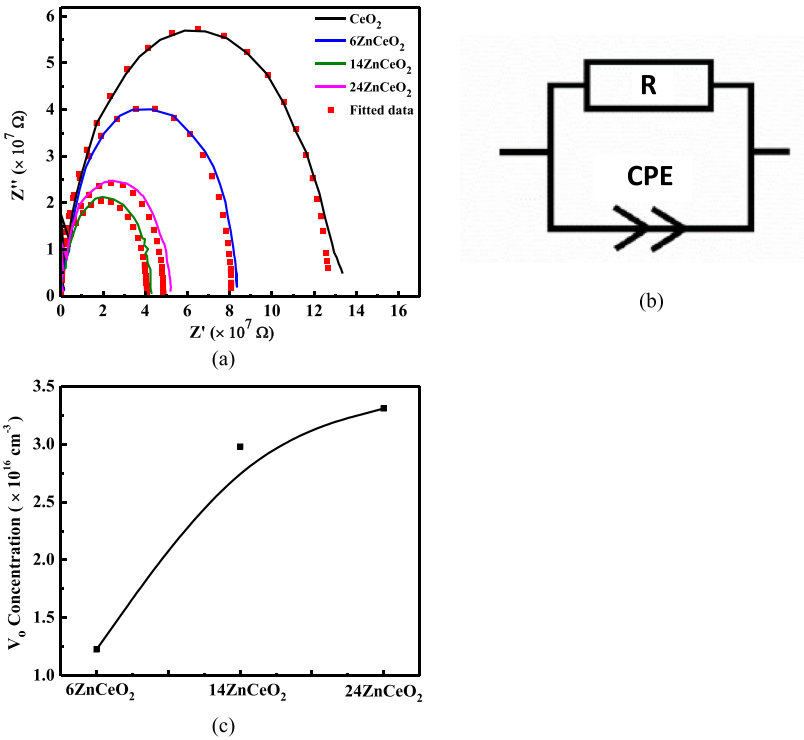

Figure 4. (**a**) Electrochemical impedance spectra of un-doped and Zn-doped CeO_2 measured in atmosphere at 250 °C. (**b**) Equivalent circuit to analyze the resistance 'R' and constant phase element 'CPE'. (**c**) Variation in concentration of V_o at different doping levels.

Composition	R (Ω)	CPE ($F.S^{(\alpha-1)}$)	α
CeO_2	1.27×10^7	5.48×10^{-10}	0.964
$6ZnCeO_2$	8.03×10^7	4.44×10^{-10}	0.934
$14ZnCeO_2$	4.08×10^7	2.63×10^{-10}	0.927
$24ZnCeO_2$	4.81×10^7	3.33×10^{-10}	0.932

Table 1. Parameters extracted from the fitted data using experimentally obtained EIS spectra with equivalent circuit, for undoped and doped CeO_2 with different doping levels.

doping concentrations, conductivity is reduced due to decreasing mobility of isolated V_o by the increased number density of the clusters. The isolated V_o gets trapped in these $(Zn, V_o)^{\times}$ defect clusters and affects the conductivity of the heavily doped sample[8,43,44].

The performance of memory devices is associated with the movement of oxygen ions through V_o, under the influence of external electric field. The resistive switching characteristics of these devices are strongly affected by the concentration of the isolated oxygen vacancies or clustered oxygen vacancies. The concentration of isolated V_o can be obtained by utilizing the chemical capacitance C_{chem} extracted by the impedance spectroscopy[42]. The relationship between the concentration of V_o in the doped CeO_2 film and the C_{chem} extracted by the impedance spectroscopy is explored by D. Chen *et al.*[42]. The chemical capacitance is defined as a measure of material's chemical storage ability under the influence of applied potential as follows:

$$C_{chem} = -\frac{8q^2V_{film}}{kT}\left(pO_2\frac{\partial[V_O^{\cdot\cdot}]}{\partial pO_2}\right), \tag{2}$$

where q, V_{film}, and pO_2 are the charge of an electron, volume of the film, and partial pressure of oxygen, respectively. In the case of doped CeO_2 thin films, it represents the formation and annihilation of V_o, due to the change in oxygen partial pressure. We considered only low pO_2, because the CeO_2 films in our case were grown in low pO_2. For low pO_2, $[V_o^{\cdot}]$ could be estimated from the measurement of C_{chem} by utilizing the following equation[44]:

$$C_{chem} = \frac{q^2V_{film}}{kT}([Pr_{Ce}]_{total} - 2[V_o^{\cdot}]), \tag{3}$$

where $[Pr_{Ce}]_{total}$ is the total doping concentration of Pr in a CeO_2 thin film. Equation 3 corresponds to the trivalent dopant in CeO_2. A similar equation was derived for bivalent dopant at low pO_2 by replacing the the mass action

relation of the trivalent dopant by mass action relation of the bivalent dopant. The mass action or equilibrium equation of Zn-doped CeO_2 is expressed in Eq. S2 in Supporting information S2. Mass and site conservation reactions are given by[42]

$$[Zn''_{Ce}] + [Zn^{\times}_{Ce}] = [Zn_{Ce}]_{total}, \tag{4}$$

where $[Zn_{Ce}]_{total}$ is the total doping concentration of Zn in CeO_2 thin films. For low pO_2, the electroneutrality and mass balance relation in Equation S4 takes on the following approximation

$$[Zn''_{Ce}] = [V^{\cdot\cdot}_{o}] - \frac{1}{2}[Ce'_{Ce}] \approx [Zn_{Ce}]_{total} \tag{5}$$

It is considered that concentration of holes and Ce vacancies are negligibly small and ignored at present situation. Equation 4 can be rewritten as follows by substituting the value of $[Zn''_{Ce}]$ from Eq. 5

$$[Zn^{\times}_{Ce}] \approx [Zn_{Ce}]_{total} - [V^{\cdot\cdot}_{o}] + \frac{1}{2}[Ce'_{Ce}] \tag{6}$$

Substituting the values of $[Zn''_{Ce}]$ and $[Zn^{\times}_{Ce}]$ from Eqs. 5 and 6 in Equation S2 yields

$$\frac{[Zn_{Ce}]_{total}\left\{[Zn_{Ce}]_{total} + \frac{1}{2}[Ce'_{Ce}]\right\}pO_2^{1/2}}{\left\{[Zn_{Ce}]_{total} - [V^{\cdot\cdot}_{o}] + \frac{1}{2}[Ce'_{Ce}]\right\}[O^{\times}_{O}]} = K_{Zn} \tag{7}$$

Rearranging Eq. 7 yields

$$[Zn_{Ce}]_{total} + \frac{1}{2}[Ce'_{Ce}] - [V^{\cdot\cdot}_{o}] = \frac{\{[Zn_{Ce}]_{total}\}^2 + \frac{1}{2}[Zn_{Ce}]_{total}\,[Ce'_{Ce}]\}pO_2^{1/2}}{K_{Zn}[O^{\times}_{O}]} \tag{8}$$

Taking derivative of Eq. 8 w.r.t pO_2

$$\frac{\partial[V^{\cdot\cdot}_{O}]}{\partial pO_2} = -\frac{1}{2}\frac{\{[Zn_{Ce}]_{total}\}^2 + \frac{1}{2}[Zn_{Ce}]_{total}\,[Ce'_{Ce}]\Big\}pO_2^{-1/2}}{K_{Zn}[O^{\times}_{O}]} \tag{9}$$

Putting the value of $\frac{\partial[V^{\cdot\cdot}_{O}]}{\partial pO_2}$ from Eq. 9 in Eq. 3 and rearranging yields

$$C_{chem} = \frac{4q^2V_{film}[Zn_{Ce}]_{total}\}^2 + \frac{1}{2}[Zn_{Ce}]_{total}\,[Ce'_{Ce}]\Big\}pO_2^{1/2}}{kTK_{Zn}[O^{\times}_{O}]} \tag{10}$$

Substituting Eq. 8 in Eq. 10 yields,

$$C_{chem} = \frac{4q^2V_{film}}{kT}\left([Zn_{Ce}]_{total} + \frac{1}{2}[Ce'_{Ce}] - [V^{\cdot\cdot}_{o}]\right) \tag{11}$$

Equation 11 represents the relationship between the concentration of isolated V_o in Zn-doped CeO_2 films and chemical capacitance extracted by the EIS. If the doping concentration of Zn ($[Zn_{Ce}]_{total}$) and the concentration of reduced Ce^{3+} ($[Ce'_{Ce}]$) is known in the Zn-doped CeO_2 thin films, the concentration of V_o can be extracted.

$[Zn_{Ce}]_{total}$ and $[Ce'_{Ce}]$ can be calculated from XPS data as follows assuming the cross-section of each elemental peak is the same[45]:

$$[Zn_{Ce}]_{total} = \frac{A_{Zn}/S_{Zn}}{\sum A_i/S_i}, \tag{13}$$

$$[Ce'_{Ce}] = \frac{A_{Ce^{+3}}/S_{Ce^{+3}}}{\sum A_i/S_i}, \tag{14}$$

$$\sum A_i/S_i = \frac{A_{Zn}}{S_{Zn}} + \frac{A_{Ce^{+3}}}{S_{Ce^{+3}}} + \frac{A_{O2}}{S_{O2}}, \tag{15}$$

where A_{Zn}, $A_{Ce^{+3}}$ and A_{O2} are the areas of Zn, Ce^{3+} and O_2 peaks in XPS spectra, respectively, and the S_{Zn} (31.861), $S_{Ce^{+3}}$ (61.447) and S_{O2} (2.881) are the atomic sensitivity factors of Zn, Ce^{3+} and O_2, respectively. The volume of the film was calculated to be 2 cm × 2 cm × 50 nm (length × width × thickness). The calculated values of $[V^{\cdot\cdot}_{o}]$ for different doping concentrations of Zn is plotted in Fig. 4(c). As can be seen in Fig. 4(c), the concentration of isolated V_o increases with the increase in doping concentration which was consistent with the increase in the conductivity of $6ZnCeO_2$ and $14ZnCeO_2$. However, there was a minute increase in the concentration of V_o on further increasing the doping concentration from 14% to 24%. As previously explained, in heavily doped samples, the

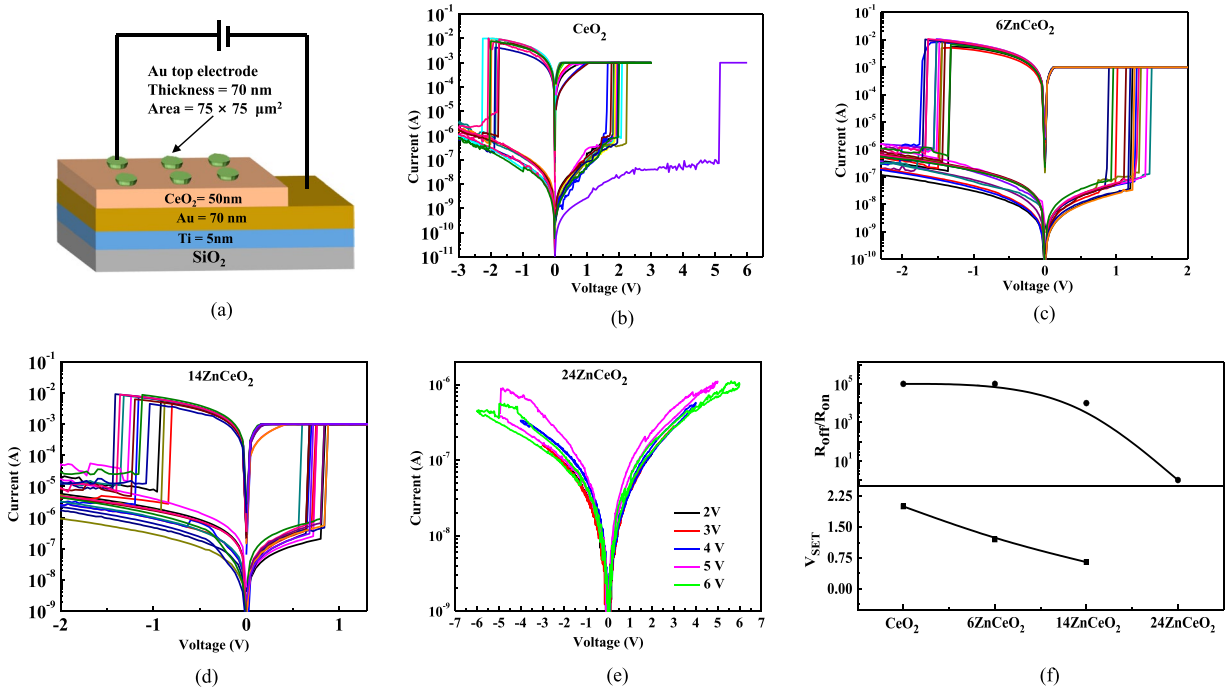

Figure 5. I–V characteristics for (**a**) un-doped CeO2 (**b**) 6ZnCeO$_2$ (**c**) 14ZnCeO$_2$ (**d**) 24ZnCeO$_2$, and (**e**) Plot of variation in R_{off}/R_{on} ratio and V_{SET} on increasing the doping concentration.

association between V_o and dopant becomes strong, and the isolated V_o gets trapped in the $(Zn, V_o)^{\times}$ clusters. This phenomenon does not allow V_o to increase considerably in heavily doped sample.

Figure 5 shows the I–V characteristics for (b) the un-doped CeO_2 (c) the 6ZnCeO$_2$ (d) the 14ZnCeO$_2$ (e) the 24ZnCeO$_2$, respectively, with (a) the schematic diagram of Au/Zn-doped CeO_2/Au devices. Figure 5(f) shows the R_{off}/R_{on} ratio and V_{SET} on increasing the doping concentration. Both R_{off}/R_{on} ratio and V_{SET} decreases on increasing the doping concentration. In order to initiate the resistive switching in undoped CeO_2, the electrical forming step was applied to the sample. Figure 5(b) presents the electroforming curve and subsequent bipolar resistive switching curves of the CeO_2 film. The electroforming occurred at 5.2 V. After the electroforming step, the device showed a typical resistive switching behavior with reliable repeatability of the switching cycles.

In the SET process, the device is first driven from the high resistance state (HRS) or the OFF state toward the low resistive state (LRS) or the ON state by applying a positive bias on the top electrode (Au) as shown in Fig. 5(a). The voltage at which the sharp increase in current is observed is termed as V_{SET}. When the negative voltage is applied at the top electrode, the process is reversed. This transition of device from LRS to HRS at a particular voltage (V_{RESET}), is referred as the RESET process. Without doping in the CeO_2, the IV curves showed high operating voltage. According to the Raman, XPS, and EIS spectroscopies, which was for the case of the un-doped CeO_2, the oxygen vacancy level was low. Hence, a large value of voltage was required to induce resistive switching was ascribed to the low level of oxygen vacancy concentration.

In the doped CeO_2, the forming step was not necessary since there was already a significant amount of V_o. Typically, the forming process is introduced to create defects to initiate resistive switching. At low Zn doping concentration, a reduction in V_{SET} was observed as shown in Fig. 5(c), which shows the effect of easy oxygen ionic motion. As a result, lower operating voltage was observed for the 6ZnCeO$_2$ device. The on/off ratio up to 10^5 was maintained for a doping concentration of 6% Zn. The 14% Zn doping concentrations resulted in a more pronounced reduction in operating voltage. However, with this doping range, the on/off ratio was reduced to 10^4. We interpreted this finding by the increased mobility of the oxygen ions due to increased oxygen vacancies. This result is consistent with the XPS and Raman spectroscopy indicating the increase in Ce^{3+} ions and V_o related Raman modes by increasing dopant concentration. By further increasing the doping concentration up to 24%, the resistive switching was diminished. At higher doping concentrations, bulk conductivity was reduced due to decreasing mobility of the isolated V_o by the increased number density of the $(Zn, V_o)^{\times}$defect clusters. At low doping concentrations, the isolated V_o existed in the CeO_2 lattice but as the doping concentration increased, the number of isolated V_o increased and the association between the defects and V_o also occurred and formed neutral or charged clusters. The size and number density of these $(Zn, V_o)^{\times}$ defect clusters increased slightly with the doping concentration. When their number density was small at intermediate doping (Fig. 6(a)), it was energetically more favorable for the oxygen vacancies to rearrange and initiate further reduction in operating voltage at intermediate doping concentrations. At high doping concentrations (Fig. 6(b)), when the size and number density of these clusters increased, these clusters caused hindrance in the mobility of the V_o. When these V_o are trapped by the defect clusters, it makes it difficult for the oxygen ions to hop over the vacancies. Hence, the mobility of the oxygen ions will be reduced. Figure 5(f) shows the results for the V_{SET} and the R_{off}/R_{on} ratio for the different Zn

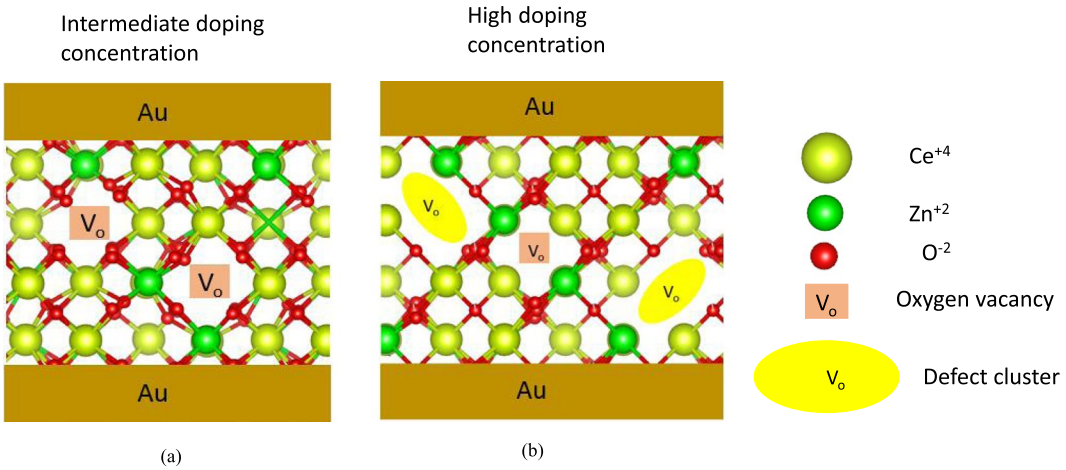

Figure 6. Representation of isolated and cluster defects at various doping levels.

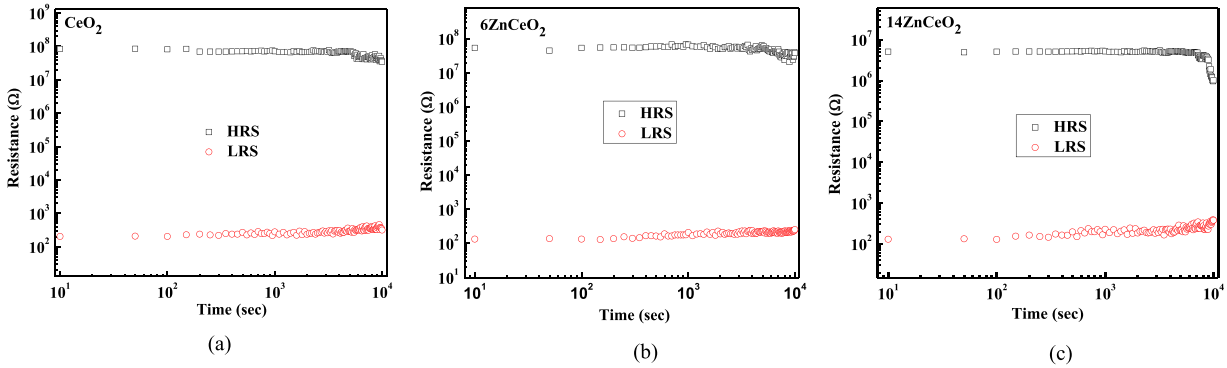

Figure 7. Retention data of (**a**) un-doped CeO_2 (**b**) $6ZnCeO_2$, and (**c**) $14ZnCeO_2$ devices in the LRS (hollow circles) and HRS (hollow squares) at room temperature.

concentrations. A maximum in the V_{SET} was observed for the device without doping. The V_{SET} was minimum at an intermediate Zn doping concentration. At high Zn doping concentrations, resistive switching was diminished. Similarly, a decrease in the R_{off}/R_{on} ratio was observed for the intermediate Zn doping concentrations. Comparing these results to the ionic conductivity, we demonstrated that there is a connection between the ionic conductivity of the oxide and the switching characteristics such as V_{SET} and R_{off}/R_{on} in resistive switching devices. This reduction in the R_{off}/R_{on} ratio and the V_{SET} was ascribed to the increase in ionic conductivity by increasing the doping concentration from 6% to 14%. The association of ionic conductivity of the Zn-doped CeO_2 with different Zn concentrations is explained in relation to the impedance spectroscopy analysis. The device to device variation of undoped CeO2, 6ZnCeO2, and 14ZnCeO2 is given in Figure S5. The statistical data indicate that there is no significant variation in the V_{SET}.

The retention measurement results of the un-doped CeO_2, $6ZnCeO_2$, and $14ZnCeO_2$ devices at room temperature by applying reading bias of + 0.2 V are shown in Fig. 7(a–c). The R_{off}/R_{on} ratio was maintained at 10^5 with no significant degradation in resistance after 10^4 sec in the un-doped CeO_2, and $6ZnCeO_2$. However, the on/off ratio was reduced to 10^4 in the $14ZnCeO_2$ device. This decrease in the R_{off}/R_{on} ratio was associated with the increase in ionic conductivity of oxygen ions by increasing the doping concentration from a 6% to a 14% doping concentration as illustrated in Fig. 5(f), which caused low R_{off}/R_{on} ratio. Zn-doped CeO_2 devices with the intermediate doping level showed a great potential for nonvolatile memory applications with the low V_{SET}/V_{RESET}, high R_{off}/R_{on} ratio, and good retention characteristics.

The endurance data for un-doped CeO_2, $6ZnCeO_2$, and $14ZnCeO_2$ are given in Figure S7. The R_{off}/R_{on} ratio of CeO_2 and $6ZnCeO_2$ devices was maintained at 10^5 without any significant degradation up to 250 cycles. Although the on/off ratio of $14ZnCeO_2$ device was reduced to 10^4, no degradation of R_{off}/R_{on} ratio was observed.

Conclusions

Zn-doped CeO_2 active layer is utilized for resistive switching. Raman spectroscopy is employed to study the structural modification introduced by the dopant in the host lattice of CeO_2. An increase in FWHM of the characteristics peak of CeO_2 (460 cm^{-1}) and the enhancement of the defect related peak (560 cm^{-1}) confirms the uniform doping of Zn in CeO_2 and the existence of $(Zn, V_o)^{\times}$ defect clusters in Zn-doped CeO_2. Increased doping of Zn in

CeO_2 leads to the formation of more oxygen vacancies in Zn doped CeO_2. Increase in oxygen vacancies with an increasing doping concentration results in reduction of operating voltage in $6ZnCeO_2$ and $14ZnCeO_2$ devices as compared to a CeO_2 device. A further increase in the doping concentration leads to the diminishing of resistive switching behavior in a 24CZnO device. This behavior is explained by the increased number density of $(Zn, V_o)^{\times}$ defect clusters which decrease the mobility of V_o in the highly doped CeO_2.

Received: 25 July 2019; Accepted: 2 December 2019;
Published online: 18 December 2019

References

1. Chua, L. O. & Kang, S. M. Memristive devices and systems. *Proceedings of the IEEE* **64**, 209–223 (1976).
2. Strukov, D. B., Snider, G. S., Stewart, D. R. & Williams, R. S. The missing memristor found. *nature* **453**, 80 (2008).
3. Ielmini, D. & Milo, V. Physics-based modeling approaches of resistive switching devices for memory and in-memory computing applications. *Journal of Computational Electronics* **16**, 1121–1143 (2017).
4. Kilner, J. A. & Burriel, M. Materials for intermediate-temperature solid-oxide fuel cells. *Annual Review of Materials Research* **44**, 365–393 (2014).
5. Andersson, D. A., Simak, S. I., Skorodumova, N. V., Abrikosov, I. A. & Johansson, B. Optimization of ionic conductivity in doped ceria. *Proceedings of the National Academy of Sciences* **103**, 3518–3521 (2006).
6. Balducci, G., Islam, M. S., Kašpar, J., Fornasiero, P. & Graziani, M. Reduction process in CeO_2–MO and CeO_2–M_2O_3 mixed oxides: a computer simulation study. *Chemistry of materials* **15**, 3781–3785 (2003).
7. Lucid, A. K., Keating, P. R., Allen, J. P. & Watson, G. W. Structure and Reducibility of CeO_2 Doped with Trivalent Cations. *The Journal of Physical Chemistry C* **120**, 23430–23440 (2016).
8. Li, Z.-P., Mori, T., Zou, J. & Drennan, J. Defects clustering and ordering in di-and trivalently doped ceria. *Materials Research Bulletin* **48**, 807–812 (2013).
9. Younis, A., Chu, D., Mihail, I. & Li, S. Interface-engineered resistive switching: CeO_2 nanocubes as high-performance memory cells. *Acs Appl Mater Inter* **5**, 9429–9434 (2013).
10. Ismail, M. *et al*. Forming-free bipolar resistive switching in nonstoichiometric ceria films. *Nanoscale research letters* **9**, 45 (2014).
11. Yang, S.-M. *et al*. Cerium oxide nanocrystals for nonvolatile memory applications. *Applied Physics Letters* **91**, 262104 (2007).
12. Lin, C.-Y., Lee, D.-Y., Wang, S.-Y., Lin, C.-C. & Tseng, T.-Y. Reproducible resistive switching behavior in sputtered CeO_2 polycrystalline films. *Surface and Coatings Technology* **203**, 480–483 (2008).
13. Younis, A., Chu, D. & Li, S. Oxygen level: the dominant of resistive switching characteristics in cerium oxide thin films. *Journal of Physics D: Applied Physics* **45**, 355101 (2012).
14. Rana, A. M. *et al*. Endurance and cycle-to-cycle uniformity improvement in tri-layered CeO 2/Ti/CeO 2 resistive switching devices by changing top electrode material. *Scientific reports* **7**, 39539 (2017).
15. Dou, C. *et al*. Resistive switching behavior of a CeO_2 based ReRAM cell incorporated with Si buffer layer. *Microelectronics Reliability* **52**, 688–691 (2012).
16. Liao, Z. *et al*. Electrode engineering for improving resistive switching performance in single crystalline CeO2 thin films. *Solid State Electron* **72**, 4–7 (2012).
17. Kehoe, A. B., Scanlon, D. O. & Watson, G. W. Role of lattice distortions in the oxygen storage capacity of divalently doped CeO_2. *Chemistry of materials* **23**, 4464–4468 (2011).
18. Khan, M. M., Khan, W., Ahamed, M. & Alhazaa, A. N. Microstructural properties and enhanced photocatalytic performance of Zn doped CeO_2 nanocrystals. *Scientific reports* **7**, 12560 (2017).
19. Ismail, M. *et al*. Improved endurance and resistive switching stability in ceria thin films due to charge transfer ability of Al dopant. *ACS applied materials & interfaces* **8**, 6127–6136 (2016).
20. Ismail, M., Ahmed, E., Rana, A. M., Talib, I. & Nadeem, M. Y. Coexistence of bipolar and unipolar resistive switching in Al-doped ceria thin films for non-volatile memory applications. *Journal of Alloys and Compounds* **646**, 662–668 (2015).
21. Kellici, S. *et al*. High-throughput continuous hydrothermal flow synthesis of Zn–Ce oxides: unprecedented solubility of Zn in the nanoparticle fluorite lattice. *Philosophical Transactions of the Royal Society A: Mathematical, Physical and Engineering Sciences* **368**, 4331–4349 (2010).
22. Liu, Y. *et al*. Superionic conductivity of Sm^{3+}, Pr^{3+}, and Nd^{3+} triple-doped ceria through bulk and surface two-step doping approach. *ACS applied materials & interfaces* **9**, 23614–23623 (2017).
23. Kim, D. J. Lattice Parameters, Ionic Conductivities, and Solubility Limits in Fluorite-Structure MO2 Oxide [M= Hf^{4+}, Zr^{4+}, Ce^{4+}, Th^{4+}, U^{4+}] Solid Solutions. *Journal of the American Ceramic Society* **72**, 1415–1421 (1989).
24. Park, D., Griffith, J. & Nowick, A. Oxygen-ion conductivity and defect interactions in yttria-doped ceria. *Solid State Ionics* **2**, 95–105 (1981).
25. Islam, M. S. & Davies, R. A. Atomistic study of dopant site-selectivity and defect association in the lanthanum gallate perovskite. *Journal of Materials Chemistry* **14**, 86–93 (2004).
26. Lee, W., Chen, S.-Y., Tseng, E., Gloter, A. & Chen, C.-L. Study of Defect Structure in Ferromagnetic Nanocrystalline CeO_2: Effect of Ionic Radius. *The Journal of Physical Chemistry C* **120**, 14874–14882 (2016).
27. Kilner, J. Defects and conductivity in ceria-based oxides. *Chemistry Letters* **37**, 1012–1015 (2008).
28. Andersson, D. A., Simak, S. I., Skorodumova, N. V., Abrikosov, I. A. & Johansson, B. Optimization of ionic conductivity in doped ceria. *Proceedings of the National Academy of Sciences of the United States of America* **103**, 3518–3521 (2006).
29. Muthukkumaran, K., Bokalawela, R., Mathews, T. & Selladurai, S. RETRACTED ARTICLE: Determination of dopant of ceria system by density functional theory. *Journal of materials science* **42**, 7461–7466 (2007).
30. Deshpande, S., Patil, S., Kuchibhatla, S. V. & Seal, S. Size dependency variation in lattice parameter and valency states in nanocrystalline cerium oxide. *Applied Physics Letters* **87**, 133113 (2005).
31. Jin, F., Shen, Y., Wang, R. & He, T. Double-perovskite $PrBaCo_2/3Fe_2/3Cu_2/3O_{5+\delta}$ as cathode material for intermediate-temperature solid-oxide fuel cells. *Journal of Power Sources* **234**, 244–251 (2013).
32. Yang, N. *et al*. Role of associated defects in oxygen ion conduction and surface exchange reaction for epitaxial samaria-doped ceria thin films as catalytic coatings. *ACS applied materials & interfaces* **8**, 14613–14621 (2016).
33. Schweiger, S., Kubicek, M., Messerschmitt, F., Murer, C. & Rupp, J. L. A microdot multilayer oxide device: let us tune the strain-ionic transport interaction. *ACS nano* **8**, 5032–5048 (2014).
34. Ackermann, S. *et al*. Kinetics of CO_2 reduction over nonstoichiometric ceria. *The Journal of Physical Chemistry C* **119**, 16452–16461 (2015).
35. Shi, Y., Bork, A. H., Schweiger, S. & Rupp, J. L. M. The effect of mechanical twisting on oxygen ionic transport in solid-state energy conversion membranes. *Nature materials* **14**, 721 (2015).
36. Rupp, J. L. *et al*. Scalable oxygen-ion transport kinetics in metal-oxide films: impact of thermally induced lattice compaction in acceptor doped ceria films. *Advanced Functional Materials* **24**, 1562–1574 (2014).

37. Taniguchi, T. *et al*. Identifying defects in ceria-based nanocrystals by UV resonance Raman spectroscopy. *The Journal of Physical Chemistry C* **113**, 19789–19793 (2009).
38. Guo, M., Lu, J., Wu, Y., Wang, Y. & Luo, M. UV and visible Raman studies of oxygen vacancies in rare-earth-doped ceria. *Langmuir* **27**, 3872–3877 (2011).
39. Guo, X., Sigle, W. & Maier, J. Blocking Grain Boundaries in Yttria-Doped and undoped ceria ceramics of high purity. *Journal of the American Ceramic Society* **86**, 77–87 (2003).
40. Göbel, M. C., Gregori, G., Guo, X. & Maier, J. Boundary effects on the electrical conductivity of pure and doped cerium oxide thin films. *Physical Chemistry Chemical Physics* **12**, 14351–14361 (2010).
41. Göbel, M. C., Gregori, G. & Maier, J. Mixed conductivity in nanocrystalline highly acceptor doped cerium oxide thin films under oxidizing conditions. *Physical Chemistry Chemical Physics* **13**, 10940–10945 (2011).
42. Chen, D., Bishop, S. R. & Tuller, H. L. Non-stoichiometry in Oxide Thin Films: A Chemical Capacitance Study of the Praseodymium-Cerium Oxide System. *Advanced Functional Materials* **23**, 2168–2174 (2013).
43. Pijolat, M., Prin, M., Soustelle, M., Touret, O. & Nortier, P. Thermal stability of doped ceria: experiment and modelling. *Journal of the Chemical Society, Faraday Transactions* **91**, 3941–3948 (1995).
44. Li, Z.-P. *et al*. Cerium-reduction-induced defects clustering, ordering, and associated microstructure evolution in yttrium-doped ceria. *The Journal of Physical Chemistry C* **116**, 5435–5443 (2012).
45. Jabłoński, A. Quantitative surface analysis by X-ray photoelectron spectroscopy. *Polish Journal of Chemistry* **74**, 1533–1566 (2000).

Acknowledgements

This research was supported by the Basic Research Program (2016R1D1A1B01009537) and the Nano Material Technology Development Program (2015M3A7B7045496,) through the National Research Foundation of Korea (NRF) funded by the Ministry of Science, ICT & Future Planning. This research was supported by the MOTIE (Ministry of Trade, Industry & Energy (10080581) and KSRC (Korea Semiconductor Research Consortium) support program for the development of the future semiconductor device. This research was supported by Korea Electric Power Corporation (Grant number: R19XO01-17).

Author contributions

S.R. and D.K. planned the project and wrote the manuscript. S.R. worked on device fabrication, device characterization and data collection. H.K. and M.F.K. helped in device fabrication and experimental measurements. D.K., J.H.H. and A.D.L. analyzed and conducted the interpretation of the results. All authors discussed the development of research and reviewed the manuscript in detail.

Competing interests

The authors declare no competing interests.

Additional information

Supplementary information is available for this paper at https://doi.org/10.1038/s41598-019-55716-4.

Correspondence and requests for materials should be addressed to D.-k.K.

Reprints and permissions information is available at www.nature.com/reprints.

Publisher's note Springer Nature remains neutral with regard to jurisdictional claims in published maps and institutional affiliations.